DTT toroidal field conductor samples test in Sultan: DC and AC characterization

DTT toroidal field conductor samples test in Sultan: DC and AC characterization

OPEN ACCESS
IOP Publishing
Superconductor Science and Technology
Supercond. Sci. Technol. **37** (2024) 075009 (13pp)
https://doi.org/10.1088/1361-6668/ad4d5e

DTT toroidal field conductor samples test in Sultan: DC and AC characterization

C Fiamozzi Zignani[1,*], G De Marzi[1], G Scarantino[2], A Di Zenobio[1], L Muzzi[1], S Turtù[1], R Bonifetto[2], A Zappatore[2], G M Polli[1,3], G Ramogida[1,3], H Bajas[4], M Ortino[4] and K Sedlak[4]

[1] ENEA, Via Enrico Fermi 45, 00044 Frascati, Rome, Italy
[2] NEMO Group, Dipartimento Energia, Politecnico di Torino, Corso Duca degli Abruzzi 24, Torino, Italy
[3] DTT S. c. a r. l., Via Enrico Fermi 45, 00044 Frascati, Rome, Italy
[4] École Polytechnique Fédérale de Lausanne (EPFL), Swiss Plasma Center (SPC), 5232 Villigen PSI, Switzerland

E-mail: chiarasole.zignani@enea.it

Received 7 February 2024, revised 6 May 2024
Accepted for publication 19 May 2024
Published 7 June 2024

Abstract

The superconducting magnet system of the Divertor Tokamak Test (DTT) facility, composed of 18 toroidal field (TF) coils, 6 poloidal field coils and a central solenoid, has been designed and many procurements have been launched. Some manufacturing aspects and some conductor features require characterization under relevant close-to-operative conditions. To confirm the design choices in all details, cryogenic tests in qualified facilities have been foreseen. In this work, the results of the TF samples characterization at the SULTAN facility at the Swiss Plasma Centre (SPC, EPFL) are presented. The 3 week test campaign started on July the 8th, 2022. The DTT TF SULTAN sample was made of two Nb_3Sn cable-in-conduit conductor 'legs', namely 'TF-A' and 'TF-B', made with wires produced by Kiswire Advanced Technology, differing for the cabling twist pitch sequence only, and designed to work in DTT at 42.5 kA at 11.9 T peak field. The extensive characterization comprised 3000 electro-magnetic (EM) cycles and two warm-up-cool-down (WUCD) steps, and in detail it included: AC measurements on the virgin conductors, on cyclic loaded conductors and after WUCDs; DC tests at 10.85 T/42.5 kA with intermediate EM cycles at 10.85 T/45 kA before and after WUCDs; DC tests using partial Lorentz force loads, and Minimum Quench Energy tests at 9 T/42.5 kA after cycles and WUCDs. The results of the DC measurement analysis verified the design, in terms of current sharing temperature (T_{cs}) and critical current (I_c), as both samples are over the minimum acceptance values. In particular, the 'TF-A' sample, characterized by a so-called 'long twist pitch' cabling sequence, showed higher performance without any degradation with loading and WUCD cycles, whereas sample 'TF-B' presented an initial T_{cs} reduction that afterwards substantially remained unchanged. In terms of strain acting at the Nb_3Sn filaments level, this result can be described by a lower effective strain in the 'TF-A' sample. AC losses were

* Author to whom any correspondence should be addressed.

measured with a calorimetric method as a function of frequency for each series of AC sinusoidal pulsing measurements, and the characteristic coupling time constants were determined.

Keywords: DTT magnets, toroidal field coils, Nb_3Sn conductors, SULTAN tests

1. Introduction

The Divertor Tokamak Test (DTT) facility is under construction at the ENEA Research Centre of Frascati within the framework of the European Roadmap for the Realization of Fusion Energy [1, 2]. This will contribute to the development of nuclear fusion by addressing key technological issues for DEMO concerning the divertor system and optimization of power exhaust management [3]. Superconducting cables play a vital role in achieving stable high magnetic fields required in nuclear fusion power plants. Tight time, budget and resource constraints forced the magnet system design team to go through a complex path in recent years, to reach a sound and satisfactory design of the superconducting coils [4]. The technology of cable-in-conduit conductors (CICCs), cooled down by a forced flow of supercritical He gas with an inlet temperature of 4.5 K, has been chosen for its intrinsic high structural capability. Concerning the toroidal field (TF) coils, Nb_3Sn has been adopted as an industrially mature material for the 42.5 kA operative current (I_{op}) at 11.9 T peak field (B_{peak}) conditions foreseen on these coils during machine operation. Some conductor manufacturing aspects, such as for instance the precise cabling twist pitches (TP) sequence, and some conductor performance, such as the AC losses they may produce in operation, require a characterization under relevant close-to-operative conditions.

The conductor test is considered a major milestone in all superconducting magnet projects, to bridge the gap between multifilamentary strand characterization and the actual properties of large cables. To confirm the design choices in all the details, cryogenic tests of short lengths of two TF conductor prototypes were performed at the SULTAN facility at the Swiss Plasma Centre (SPC) of the École Polytechnique Fédérale de Lausanne (EPFL), in Villigen, Switzerland. The testing program was dictated by the operating mode of the magnet. The present paper, after a brief description of the DTT TF SULTAN sample, reports a detailed description of the test results and data analysis, including interpretive simulations carried out with reliable numerical tools such as the 4 C code [5].

2. DTT TF SULTAN sample

2.1. The strands

Superconducting wires supplied by Kiswire Advanced Technology (KAT) are internal-tin Nb_3Sn strands characterized by a diameter of 0.82 mm, a Cu:non-Cu = 1 and a critical current density J_{c_nonCu} (4.2 K, 12 T, 0%) $>$ 1200 A mm^{-2} [6].

Measurements carried out after heat treatment with 100 h duration at the 650 °C plateau, lied within the specification: critical current (I_c) measurements on a standard ITER barrel at 12 T in liquid helium confirm values for different billets $>$320 A; AC hysteresis losses, Q_{hyst}, measured by a vibrating sample magnetometer over a $\pm$3 T cycle at 0.5 T min^{-1}, confirmed values $<$1000 mJ cm^{-3}.

Since the Nb_3Sn wires operate in CICCs under strain [7–9], a complete characterization of the wires was carried out with the ENEA WAlters SPring (E-WASP) test facility [10], in terms of critical current as function of applied axial strain, ε_{ax}, applied magnetic field, and temperature. This allows us to reliably reconstruct the I_c performance over a wide strain–temperature–field range, based on the formulation of the ITER scaling law [11]. The parameterization of the critical surface of the DTT TF Nb_3Sn strands has been extensively described in [12], and the scaling parameters that have been used in the following analysis of the qualification sample measurements (including the numerical simulations) are reported in table 1.

2.2. The CICCs

The main parameters of the DTT TF CICC are listed in table 2 and its cross-section is shown in figure 1. The design follows the concept of a rectangular CICC without any pressure—relief channel and with relatively low void fraction. The TF coils have been designed to operate under DTT operating conditions at 42.5 kA and 11.9 T peak field [4]. The DTT TF SULTAN sample was assembled at the SULTAN test facility, joining—for measurement purposes—the two TF sections of Nb_3Sn CICCs shipped from the conductor manufacturing company, Innovation and Consulting on Applied Superconductivity. The two CICC sections (otherwise called 'legs') were identified as 'TF-A' and 'TF-B': they only differ for the twist pitch sequence of the cabling stages, which are shown in table 3. For the TF-A leg, a 'long-twist-pitch' sequence was considered [13] (i.e. with a long pitch at the first cabling stage and a 10%–15% increase in pitch length at every next stage up to the petal), whereas the cabling sequence of the TF-B is the same as that adopted for the CICCs of the NHMFL Series-Connected Hybrid Magnet [14]. Both 'TF-A' and 'TF-B' cabling sequences were chosen as they had previously demonstrated good performance during the test campaign at the SULTAN facility, as will be detailed in paragraph 4.1. The heat treatment was performed at the SPC, following the schedule provided by KAT [6]. At the SULTAN

Table 1. Fitting parameter for the Nb_3Sn strand of the DTT TF coils.

Parameters	Units	Variable *p, q*
C_0	kA T	46.59
$T_{C0,\max}$	K	16.20
$B_{C20,\max}$	T	29.10
C_{a1}	—	36.05
C_{a2}	—	0
$\varepsilon_{0,a}$	%	0.19
ε_m	%	−0.33
p	—	0.95
q	—	2.34

Table 2. DTT TF CICC design parameters.

Superconductor	Nb_3Sn
Cable layout	[(2sc + 1Cu) × 2 + (3sc)]× 3 × 3× (4 + core) × 5 (core = 3 × 4 Cu only)
SC strand diameter(Cr Plated) (mm)	0.82
Cu strand diameter (Cr plated) (mm)	0.82
No. of SC strand	420
No. of Cu strand	180
Conductor height (mm)	22.2
Conductor width (mm)	28.9
Jacket thickness (mm)	1.9

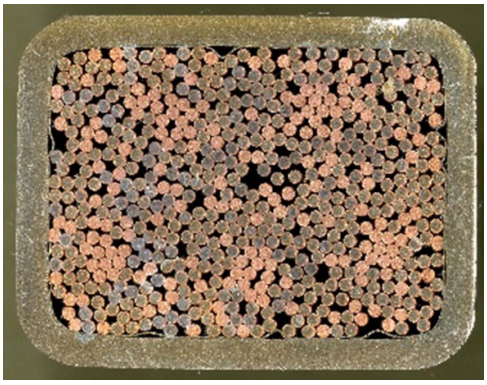

Figure 1. DTT TF SULTAN sample cross section.

Table 3. Twist pitch length of the cabling stages.

	Cabling pitch sequences (mm)
'TF-A'	100/110/125/140/300
'TF-B'	82/135/180/220/290

facility, the two upper terminations have also been manufactured, see figure 2.

3. Test description and sample instrumentation

In the SULTAN test facility, the two conductor 'legs' were joined at the bottom and electrically connected at the top to the SULTAN superconducting transformer. The sample was

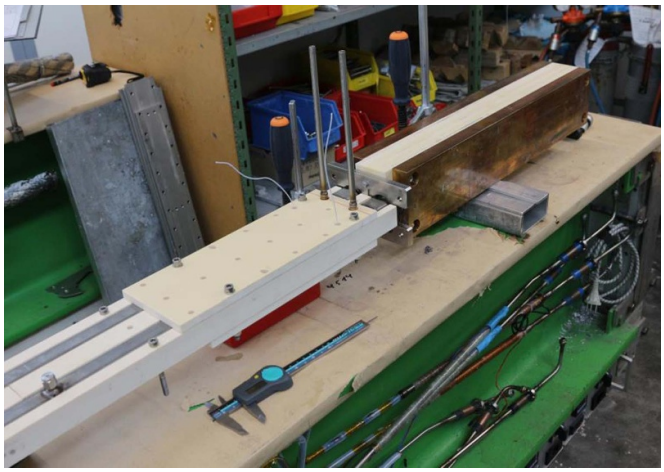

Figure 2. SULTAN sample preparation: view of the upper termination with visible insulating material in-between both legs and helium outlets to be mounted.

placed vertically in the bore of the magnetic system. A clamping system maintains the two legs in a parallel configuration, against the electro-magnetic (EM) forces. The 10.85 T peak background field, provided by the SULTAN facility, is applied to a region of the conductor that is about 0.45 m long (named here as the high field zone, HFZ) [15]. The bottom joint allows both legs to be operated by a single power supply so that the two conductors are tested simultaneously. The two legs are assembled in such a way that the EM load is exerted on the wide conductor side. They are cooled through a forced flow of supercritical helium flowing from the bottom joint to the upper terminations, flowing in parallel through the two legs. The conductors are equipped with temperature (T), voltage (V), mass flow rate ($\mathrm{d}m/\mathrm{d}t$) and pressure (P) sensors along their length, indicated in the instrumentation scheme reported in figure 3, distinguished with a specific standard nomenclature used in SULTAN. The temperature probes and voltage taps are installed on the conductor jacket. Each TF sample 'leg' is equipped with four voltage taps (VH) and temperature sensors ($T1$, $T3$ and $T2$, $T4$ for the TF-A and TF-B, respectively) pairs across the HFZ: each of them is composed of four separate sensors, one on each side of the jacket, at the same axial location. Other voltage taps are probing the bottom joint, the whole sample and the terminals, respectively. Two pressure gauges (PI) are installed on the 'TF-B' sample leg, at a distance of 2 m, to evaluate the pressure drop (ΔP) along the conductor, characterized by the absence of a preferential pressure relief channel. A pressure tap (P906) is also connected to the pressure gauge close to the He inlet, see figure 3. On the inlet branches, two independently controlled resistive heaters (R951, R952) are installed to finely control the inlet He temperature. The He flow rate in each conductor 'leg' is controlled by two separated valves (CV970, CV980) on the outlet branches. The position of the inductive AC coil is highlighted with respect to the HFZ.

The three week test campaign of the DTT TF SULTAN sample started on the 8th of July 2022. One of the main targets of the test was the performance verification of the different

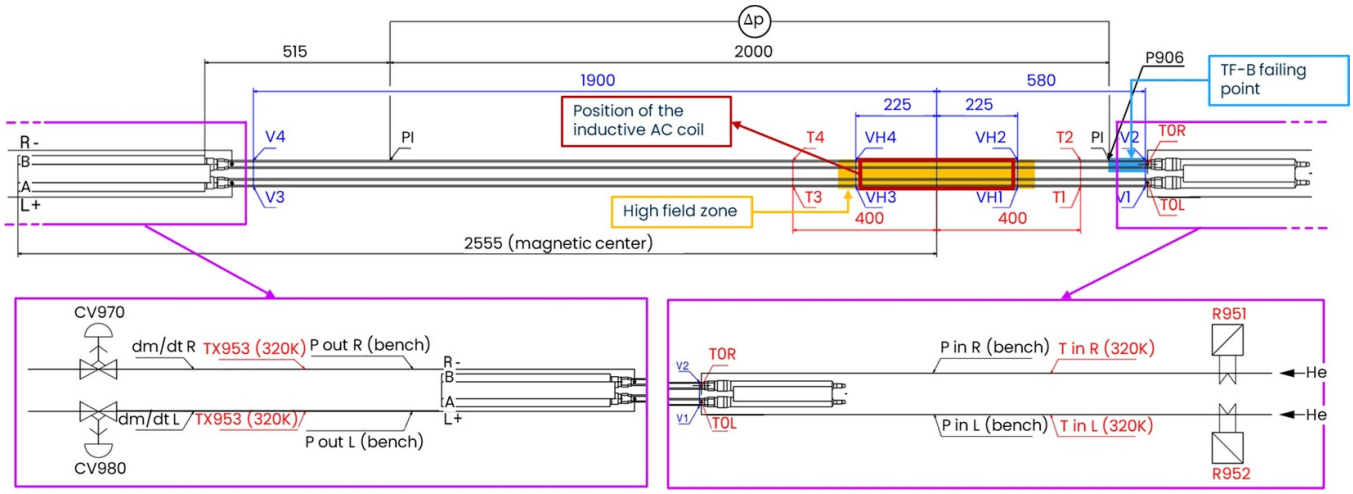

Figure 3. SULTAN sample instrumentation scheme. The location of the high field zone and of the TF-B failing point (where an odd, localized pressure drop should be present) are also reported.

cabling options. The testing program was defined with the aim of characterizing the superconducting properties in view of the DTT TF coil operating conditions and it included, after the cold instrumentation check at $B = 0$ T, the following milestones:

(a) pressure-drop measurements of virgin conductors as function of He mass flow rate, dm/dt, at 0 T, 0 kA;
(b) reference current sharing temperature (T_{cs}) tests with 10.85 T SULTAN background field and 42.5 kA sample current (considering also the conductor self-field, the magnet field value is the closest one to the operative conditions in the actual coil);
(c) 3000 EM load cycles at 10.85 T/45 kA (corresponding to the peak EM load condition in the coil, see paragraph 4.1), with T_{cs} measurements at reference conditions repeated at various steps in-between;
(d) two warm-up-cool-down (WUCD) cycles, with repetition of T_{cs} measurement at reference conditions
(e) T_{cs} tests also at different background fields;
(f) various critical current tests (I_c), for comparison with T_{cs} measurements;
(g) AC losses measured with a background field of 2 T, with a $\Delta B = \pm 0.3$ T exciting field, performed on virgin sample, after 200 EM load cycles and after 3000 EM load cycles and WUCDs;
(h) Minimum quench energy (MQE) tests at 9 T and 42.5 kA;
(i) pressure-drop measurements, after cycles/WUCD, as function of He dm/dt at 0 T, 0 kA.

The number of EM load cycles (3000) has been conservatively fixed for these tests as the one expected in case of a possible DTT operation choice based on a daily switch-off of the TF coil system at the end of operations.

For the experimental test analysis, the choice of the input data relied on the proximity of the sensors to the HFZ. The average of the four sensors data composing each of $T1$, $T3$, VH1, VH3 and $T2$, $T4$, VH2, VH4 for the TF-A and TF-B respectively, was used for the temperature and voltage evaluations. The difference between the different voltage pairs has been observed to be negligible. For the pressure data, the PI gauges on the TF-B were connected to a differential-pressure gauge for the precise pressure drop measurement along the conductor, while for the TF-A, only the standard inlet and outlet pressure sensors were used (P in L, P out L), not allowing the accurate measurement of the (small) pressure drop. The data of the mass flow rate were uniquely taken from the downstream mass flow meters (dm/dt L, dm/dt R) installed in the outer branches on each conductor outlet cryo-line (figure 3).

4. Experimental tests results in SULTAN

4.1. DC measurements

The current sharing temperature measurement, T_{cs}, at the nominal operating current and field, is one of the key tests for the qualification of the DTT conductors. The T_{cs} is in this case defined as the conductor temperature at which an average, longitudinal electric field of 10 μV m^{-1} is observed at nominal operative current $I_{op} = 42.5$ kA, in a background field of 10.85 T, corresponding, after accounting for the self-field, to 11.7 T maximum field and to about 11.3 T effective field on the SULTAN sample. It is worth noting that 11.7 T is the effective field value foreseen in the DTT TF coil system during operation. The minimum expected T_{cs}, *i.e.* the TF coil design acceptance criterion, has been extrapolated to the SULTAN working conditions, considering a design effective strain $\varepsilon_{eff} = -0.65\%$, and it is 6.38 K. Appropriate definitions of both effective field and effective strain will be given below.

The T_{cs} is evaluated by means of the electrical method based on the evaluation of the voltage drop measured along the HFZ [16]. A detailed description of the analysis procedures for the SULTAN DC and AC measurements can be found in [17, 18].

The plot of the performance variation with cyclic loading, is shown in figure 4. The T_{cs} was measured on both legs at

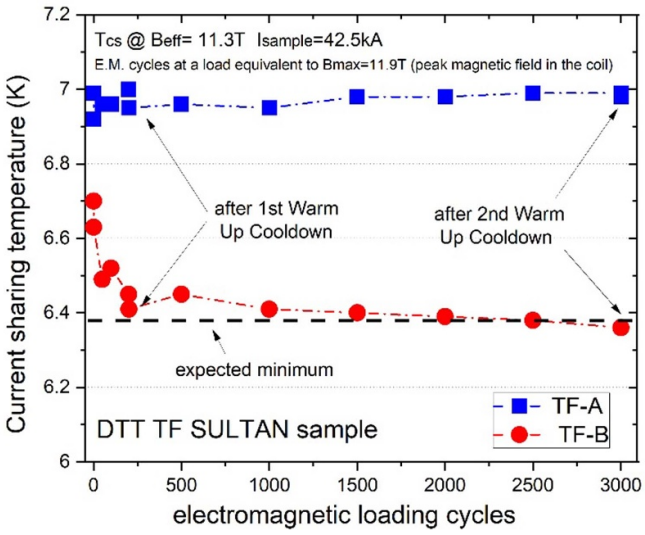

Figure 4. T_{cs} behaviour versus EM cycles for 'TF-A' and 'TF-B' sections. The black dashed line represents the minimum expected $T_{cs} = 6.38$ K, extrapolated at the SULTAN working conditions considering a design effective strain $\varepsilon_{eff} = -0.65\%$.

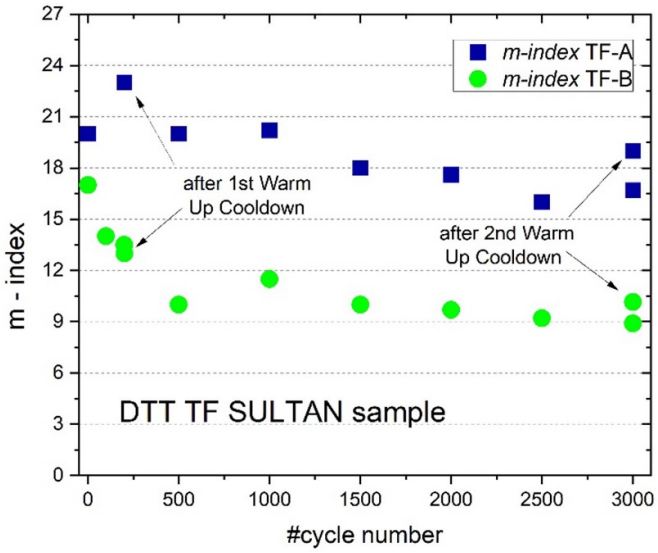

Figure 5. *M-index* behaviour versus EM cycles for 'TF-A' and 'TF-B' sections.

the reference operating conditions, repeated at different steps during the application of EM load cycles and after the first and final WUCD. The largest part of the T_{cs} variation for 'TF-B' conductor occurred within the first 200 EM cycles, while afterwards it substantially remained unchanged. 'TF-A' conductor does not show any T_{cs} degradation after two WUCDs and 3000 EM loads. The dashed black line in figure 4 represents the minimum expected T_{cs}, extrapolated at the SULTAN working conditions (42.5 kA, 10.85 T), considering a design effective strain $\varepsilon_{eff} = -0.65\%$. The 'TF-A' CICC is stable above the acceptance T_{cs} value, whereas a maximum number of loading cycles of about 2500 should be considered for the 'TF-B' CICC to be strictly above the minimum T_{cs} value.

The effective strain (ε_{eff}) is a parameter that characterizes CICCs, and that is used to fit the measurements on conductors by using the strand data [7], according to the procedure reported, for example, in [13]. As for the T_{cs}, the effective strain parameter is also influenced by both the reversible compressive and bending strain components acting at the Nb_3Sn filament level, as well as by filament breakage, and can thus be used to quantify the strand-in-CICC performance, compared to single wire tests [7, 19].

The steepness of the *Electric Field vs. Temperature* transition curves, expressed in terms of the so-called *m-index* [20], has been estimated for the *T*cs runs at the 42.5 kA–10.85 T reference conditions. A slight reduction is observed with EM cycling for 'TF-A' conductor from 20 to 17 and a larger one for 'TF-B' conductor from 17 to 9. Corresponding data are presented in figure 5. On the other hand, the *n-index* values, characterizing the steepness of the *Electric Field vs. Sample Current* transition [21], are between 7 and 13 for measured 'TF-A' currents between about 35 kA and 39 kA, and between 4 and 8 for measured 'TF-B' currents between about 30 kA and 35 kA. For comparison, the values extrapolated at the SULTAN testing conditions, from I_c *vs. strain* tests of the constituting strands [22], provided higher *n-index* values, *i.e.* in the range $17 \div 19$. It has been shown that a conductor transition *n-index* smaller than that of the corresponding single strand value is not always to be considered an indication of filament breakage [8]: a low value for the CICC *n-index* may also be associated with a reversible decrease of performance in the absence of filament fracture [23], especially when, as for 'TF-A' conductor, there is no T_{cs} depletion with cycling. These different behaviours have also been identified in the literature as 'Type 1 Degradation', due to the strain sensitivity of critical current in Nb_3Sn and inter filament current transfer, and 'Type 2 Degradation', linked to mechanically damaged filaments in the strands cross section [24].

Cable *n-index* reduction with respect to the constituting strand behaviour has been explained considering that inside these conductor strands are subject to bending strain coupled to the axial pre-compression [8, 23, 25]. When the overall strain inside the cables exceeds the limit for filament fracture, a T_{cs} degradation with EM cycling is found in addition to the *n-index* decrease. On the contrary, when there is no T_{cs} degradation, the *n-index* reduction is not to be ascribed to filament fracture but can be explained considering *n vs.* I_c curve characteristics of strands subject to bending and axial strain components [22, 26].

Figure 6 summarizes other DC test results, in terms of T_{cs} *vs* I_{op} runs (solid symbols), carried out at different background field values, after 3000 EM cycles and two WUCDs.

To estimate the effective strain ε_{eff} acting on the conductor, a 2D finite element model of the SULTAN sample section has been implemented by means of the *magnetic field* interface of the commercial software Comsol Multiphysics [27]. The average electric field, $<E>$, on the conductor sections is given by the following formula:

$$\langle E \rangle = E_c \iint \left(\frac{I_{op}}{I_c\,(B, T_{cs}, \varepsilon_{eff})} \right)^n \mathrm{d}x\,\mathrm{d}y \qquad (1)$$

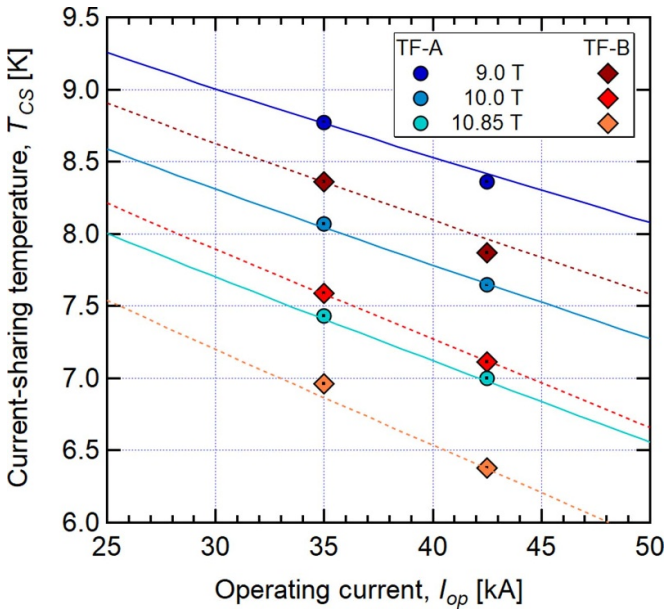

Figure 6. T_{cs} test results after 3000 EM cycles and 2 WUCDs at different electromagnetic conditions ('TF-A' solid circles, 'TF-B' solid diamonds). Lines were obtained from the I_c parameterization in which both B_{eff} and ε_{eff} are functions of I_{op} (solid and dotted lines for 'TF-A' e 'TF-B', respectively).

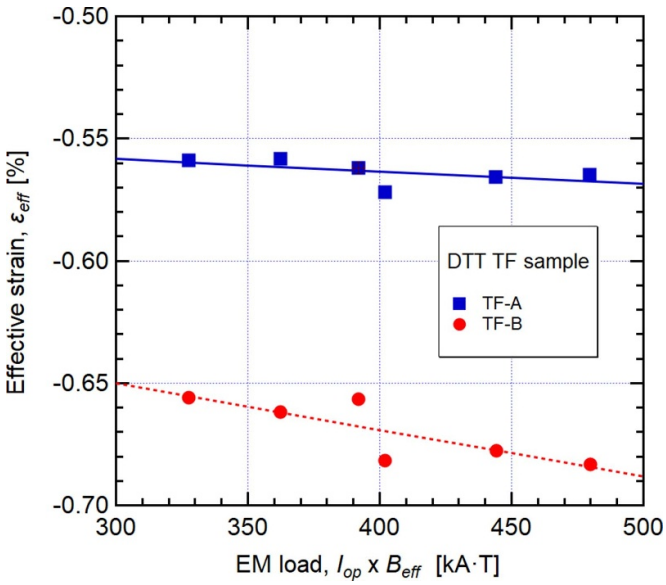

Figure 7. Effective strain after 3000 EM cycles and 2 WUCDs, plotted *vs*. effective magnetic load. Symbols (squares and circles for samples 'TF-A' and 'TF-B' respectively) are obtained for each run using the scaling law [12] to fit measured T_{cs} values using the computed local magnetic field. Lines represent the linear fits of the effective strains expressed as: $\varepsilon_{eff} = a + b\, I_{op} \times B_{eff}$, see text.

where the surface integral is performed on the entire section of the conductors, $B = B(x,y)$ is the local value of the magnetic field to be included in the parameterization of $I_c(B(x,y),T_{cs},\varepsilon_{eff})$ and n is the *n-index* value, characterizing the steepness of the *Electric Field vs. Sample Current* transition of the constituting strands. In the calculation, an n value of 12 has been used. The effective strain is calculated in such a way that the average value of the electric field in the conductor cross-section is equal to the electrical field criterion $E_c = 10\ \mu V\ m^{-1}$. Once the effective strain is known, the B_{eff} can be evaluated, for each of the measurements shown in figure 6, as the magnetic field such that $I_c(B_{eff},T_{cs},\varepsilon_{eff}) = I_{op}/N$, being $N = 420$ the number of superconducting strands. It has been found that in the SULTAN sample B_{eff} is related to the operating current by the following linear relation: $B_{eff} = B_S + K{\cdot}I_{op}$ [28], where B_S is the SULTAN background field. The K value obtained from our data is 0.010396 ± 0.000186 T/kA, with a 95% confidence interval in the error analysis. The lines plotted in figure 6 were obtained from the I_c parameterization, in which both B_{eff} and ε_{eff} are functions of I_{op}.

In figure 7, the effective strain is plotted *vs*. the effective magnetic load ($I_{op} \times B_{eff}$) for each T_{cs} measurement. It is worth noting that ε_{eff} is substantially independent from the EM load for section 'TF-A', while it slightly increases with load, in absolute value, for section 'TF-B'. Besides the exact quantification, these results reflect a different strain state of Nb_3Sn in the the two legs, with the 'TF-A' configuration offering a more stable support for constituting strands [9, 19]. The lines in figure 7 represent the linear fits of the effective strains expressed as: $\varepsilon_{eff} = a + b\, I_{op} \times B_{eff}$, where the coefficients a and b are -0.54305% and $-5.124 \times 10^{-5}\%$ for the leg 'TF-A', and -0.59307% and $-1.904 \times 10^{-4}\%$ for the leg 'TF-B'. In the investigated EM load region, for conductor 'TF-A' an overall $\varepsilon_{eff} = -0.56\%$ can be extrapolated, while for sample 'TF-B' an ε_{eff} between -0.65% and -0.69% is found. It is important to underline that there is a strain distribution inside cabled conductors [7, 29–31] and that the single effective strain value has no physical meaning but is a parameter used and useful in the conductors' design which is necessarily based on a single strand data.

The different behaviour of the two 'legs', in terms of both T_{cs} and *n-index*, is here attributed to the different distribution of the load, as a result of the different cabling pitch sequence of the two samples, see for example [9, 13, 32–35]. In particular, the difference between the initial *current sharing temperature* values measured for the two legs is consistent with what was reported in [13] about the T_{cs} dependence on the cabling twist pitch of the first stage. Concerning 'TF-A' conductor, the long twist pitch cabling sequence, together with the low void fraction and the rectangular cross-section, has been shown to lead to a favourable load distribution within the cable, corresponding to smaller ε_{eff} [32–35], which has been found to be correlated to a narrow strain distribution in the cable cross-section [35], thus resulting in a stable T_{cs} with cycling loading. A stable T_{cs} with EM cycles, is not only linked to the value of the twist pitches, but also to their reciprocal ratio, especially in the first stages [13]. Results as good as those of 'TF-A' leg, in terms of T_{cs} stability versus # EM cycles and effective strain, have been obtained, among others, by the ENEA DEMO rectangular High field [19, 34] and Low Field [32] conductors, by the EU-AltTF DEMO sample [33, 35] and by the TFPRO2 OST-2 conductor [20, 23], all cables designed with rectangular section, similar twist pitch cabling sequence

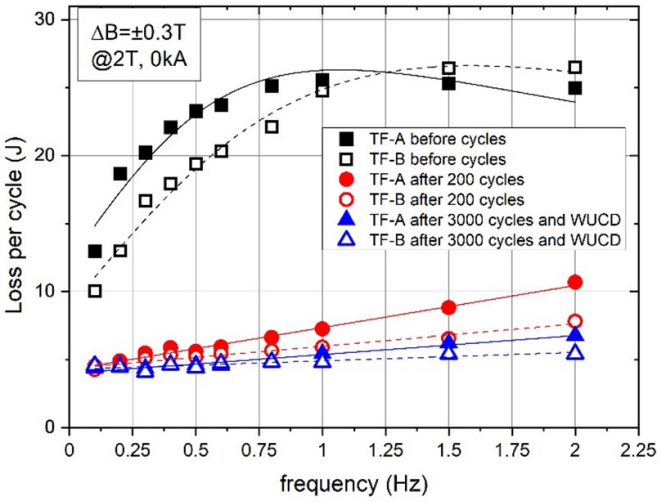

Figure 8. Symbols represent AC losses measured under a sinusoidal varying field, as a function of frequency, for both 'legs', at 2 T and without transport current, on virgin samples, after 200 EM cycles and after 3000 EM cycles and WUCDs. Lines ('TF-A' leg—continuous lines, 'TF-B' leg—dotted lines) are fits using a single time constant approximation.

(almost same ratio between pitches of the first stages) and low void fraction.

Concerning 'TF-B' conductor, even if with performance not as outstanding as those of 'TF-A', and given the different load distribution within the cables cross sections with respect to the round ITER TF CICCs, its behaviour can still be described as a Type 1 degradation, according to [24]: its T_{cs} drops of about 0.3 K within the first few hundreds EM cycles, but then remains fairly stable, very differently from what happened to the first ITER TF conductors [36, 37], which showed a typical Type 2 degradation [24]. A conductor with a similar twist pitch cabling sequence as 'TF-B' was tested in SULTAN in 2009: it was the high field section of the series-connected hybrid outsert coil of the National High Magnetic Field Laboratory (NHMFL) [38]. Only after more than 2500 EM cycles the DTT 'TF-B' conductor's performances seem to slowly decay. This last part of the test could not be predicted, as the CICCs of the NHMFL series-connected hybrid magnet was tested only for 600 EM cycles and not for 3000 EM cycles as 'TF-B' was.

4.2. AC losses

AC loss measurements were performed before EM loading of the sample and then repeated after 200 EM cycles (10.85 T/45 kA), before WUCD, and again after full EM loading (3000 cycles) and WUCDs. AC losses were assessed by He calorimetry and they were measured at 2 T and 0 kA, while AC coils were operated with a sinusoidal sweep of amplitude ±0.3 T, at different frequencies (from 0.1 Hz to 2 Hz). The symbols reported in figure 8, for both legs, refer to the total energy deposited per cycle in the region between the temperature sensors upstream and downstream of the HFZ.

AC losses on virgin samples are characterized by a peak in the measured frequency range, that shifts to frequencies higher than 2 Hz after EM cycling. It is worth noting that DTT TF coils are characterized by the absence of steel wrapping around the last-but-one cabling stage. Losses on both legs were substantially reduced by cycling, as shown in figure 8, due to the expected increase in transverse resistance. Considering the different twist pitch cabling sequence, we could have expected a larger difference between the losses of the two legs [13]. When wrapping is present around petals, the transverse resistance between superconducting (SC) strands within a petal (intra-petal resistance) is much smaller than the transverse resistance between SC strands from adjacent petals (inter-petal resistance). Without wrapping (that is our case), the inter-petal transverse resistance is of the same order of magnitude as the intra-petal transverse resistance, so that the last cabling stage dominates the loss behaviour, because coupling currents with large loops flow through neighbouring petals. In particular, the coupling time constants are dominated by the twist pitches of the last cabling stages [39, 40], which have similar values for the two legs.

Despite the different geometry and twist pitch pattern, the qualitative behaviour of the losses, before and after cycles, resembles that observed on the ITER TF CICCs [17], while concerning the quantitative behaviour the measured values are higher, possibly due to the absence of sub-cable wraps. The behaviour shown in figure 8 resembles what found for other rectangular conductors [33, 41], characterized by the presence of 'petals' wrapping but with a higher void fraction in the cable cross section (v.f. $\sim 30\% \div 28.9\%$). This is very different from what is found, e.g. for the high-field DEMO sample [34] characterized, as this DTT TF SULTAN sample, by the absence of petal wrapping around the last-but-one cable stage, but with a much lower void fraction (v.f. $\sim 24.6\%$). In this last case, the peak of the losses was in the very low frequency range, and we have not yet been able to completely explain these inconsistencies, even if it has been shown [40] that cable pattern, sub-cable wraps and void fraction significantly affect the coupling loss and, overall, could be responsible for the AC losses' curves similarities and differences.

It is well known that, in multi-stage CICCs, the different transverse resistance of the cable stages results in multiple time constants [42, 43], determined by the multiple induced current loops. Each time constant is relevant for a specific frequency range, and in general several time constants are needed in order to fit the losses *vs*. frequency curve. When a transient AC loss regime is dominant over the others, a single time constant is sufficient to describe the experimental data. In figure 8, lines represent fits obtained using the single time constant approximation [44] to match the whole measured loss curves, normalized by the volume. Coupling time constant ($n\tau$) values of 300 ms and 200 ms respectively are obtained for 'TF-A' and 'TF-B' losses on virgin samples.

The description of the experimental data obtained before cycles with a single time constant is reasonably good, in particular for the 'TF-A' conductor, thus implying that a single time-constant model is sufficient to describe the experimental data. Coupling time constants of experimental data collected

after 200 EM cycles and after 3000 EM cycles and WUCDs have been evaluated from a linear fit of the slope of the cable loss per cycle curve *vs.* frequency, normalized by the volume. The calculated $n\tau$ values are respectively 35 ms and 16 ms for 'TF-A' conductor and 15 ms and 6 ms for 'TF-B' conductor. It must be said that the lack of measurements at very low frequencies, together with with the fact that the maximum of the loss curves has shifted to higher frequencies after EM loading, could have led to an underestimation of the coupling time constants after cycles. The latter are of the same order as those previously measured on ITER TF prototype conductors [45, 46], and of the EU-AltTF conductor [33].

4.3. Stability tests

As a last item of the experimental campaign, after 3000 EM cycles and two thermal (WUCD) cycles, the MQE tests were performed, at 9 T background field, without sample current ('calibration' runs) and with a sample current of 42.5 kA, at 2.5 g s^{-1} helium mass flow rate. The energy deposited in the sample was assessed calorimetrically. Unfortunately, a quench occurred in the 'TF-B' conductor for voltages in the capacitor bank above 140 V independently from the sample temperature. Therefore, on the one hand it was not possible to measure MQE for 'TF-A' conductor, while on the other hand the MQE measured on 'TF-B' could not be considered reliable. Different hypotheses were advanced for the observed behaviour of the 'TF-B' conductor: the presence of a flow obstruction in the He inlet region (see below section 4.4 for the details) could have partially damaged the strands or the temperature increase caused by the He lamination in the flow could have resulted in a hotspot in the inlet region due to the obstruction. The energy deposited on the conductors due to the pulse of the inductive coil was calculated for both legs for the 'calibration' run and for the current runs with no quench by means of calorimetry, according to equation (2)

$$Q_{\mathrm{dep}} = \dot{m}\left(t_{\mathrm{init}}\right) \int_{t_{\mathrm{init}}}^{t_{\mathrm{fin}}} \left[h\left(t\right) - h^{0}\right] \mathrm{d}t \tag{2}$$

with Q_{dep} [J] the energy deposited, $\dot{m}\left(t_{\mathrm{init}}\right)$ $\left[\mathrm{kg\,s^{-1}}\right]$ the mass flow rate in each conductor evaluated before the pulse, $h\left(t\right)$ $\left[\mathrm{J\,kg^{-1}}\right]$ the helium enthalpy as function of time, evaluated from the standard He properties library [47] considering the average of the measured pressures and temperatures from the sensors installed in the two conductors according to the standard SULTAN instrumentation scheme for ITER samples (see again figure 3). Lastly, h^{0} $\left[\mathrm{J\,kg^{-1}}\right]$ is the average enthalpy evaluated on a stabilized time-interval before the inductive coil discharge, subtracted as an offset for the deposited energy computation. The calorimetry results are presented in figure 9.

In MQE tests, the reference values for the energy deposited on the conductors are those obtained in the 'calibration' runs. Tests performed with current are necessary to assess the minimum voltage (and therefore energy) of the inductive coil resulting in a quench in the conductor sample, but due to the joule power deposited during the quench and the AC losses associated to the current discharge, the associated calorimetry is not considered for the MQE evaluation. The effect of AC losses and joule heating is evident in figure 9, where higher energy values are observed in all the tests with current. The minimum voltage in the capacitor bank at which the quench is triggered is 140 V, as already mentioned, unexpectedly independent from any other parameter such as the initial conductor temperature. The corresponding MQE extracted from the 'calibration' runs is 2–2.5 J (i.e. 16–21 mJ cm^{-3} of cable). This value is actually not far from the MQE of NbTi conductors, as e.g. those of ITER [17, 48] and JT-60SA TF ones [49], for an operating temperature ∼0.1 K smaller than the T_{cs} (as in the present case). However, ITER Nb_3Sn conductors typically show MQEs about one order of magnitude larger [48, 50].

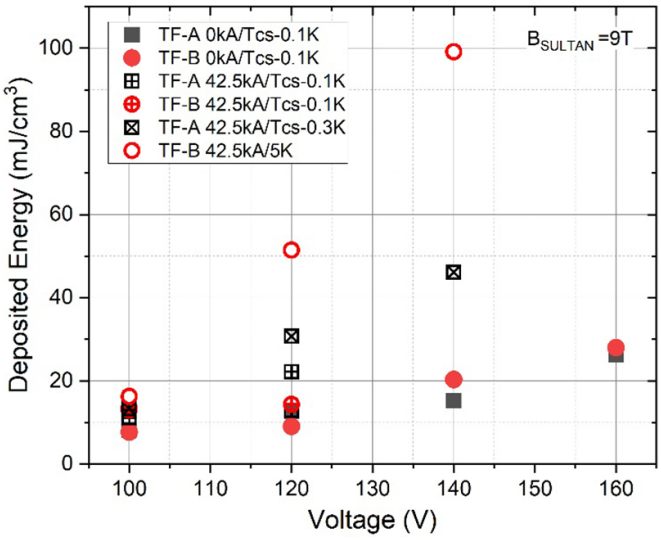

Figure 9. Calorimetrically assessed deposited energy both during calibration run and in presence of transport current on 'TF-A' (squares) and 'TF-B' (circles) conductors (the energy is expressed per unit of cable volume).

Due to the quenches of the 'TF-B' conductor, a numerical analysis with the 4 C code was performed to support the data interpretation and investigate the stability of the TF conductor samples. The 4 C code [51], the state-of-the-art tool for thermal-hydraulic simulation of transients in superconducting magnets, is being used to support the design verification of the DTT magnet system [5, 52]. Energy conservation equations employ a 1D approximation along the conductor axis, taking advantage of the de-coupling in the time scales of gradients in the transverse and axial directions.

For the modelling of the MQE tests for the 'TF-B' conductor, the simulation setup includes an implicit time scheme, an adaptive mesh refinement in the HFZ (where the inductive coil for AC and MQE tests is located) and an adaptive time step to follow the quench initiation phase. The duration of the power deposition was derived from the SULTAN inductive coil data (nominally, '*PulseBattery*'): an average value of ~ 150 *ms* is considered for the MQE tests. As boundary conditions, the mean values measured during the tests for inlet

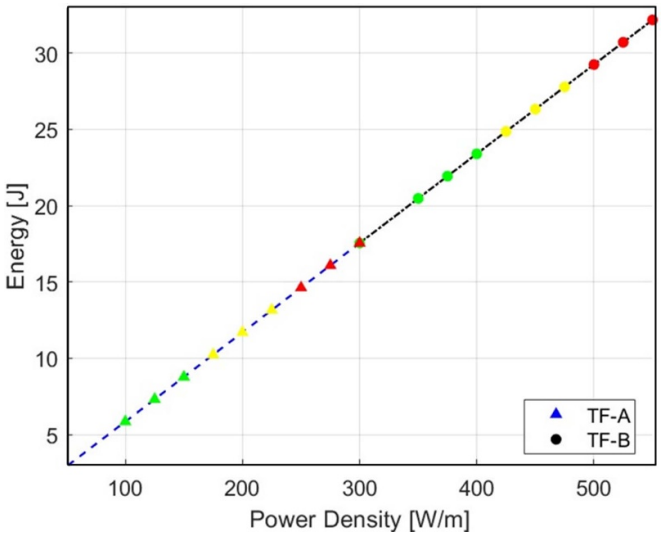

Figure 10. 4 C results of the MQE tests for the 'TF-B' conductor. In green: no quench, in yellow: quench recovery, in red: quench.

pressure and temperature and outlet pressure are imposed. The scaling parameters in [12] are adopted, while the *n-value* and the *effective strain* are obtained from the DC measurement tests at the corresponding EM load (9 T, 42.5 kA): $n = 5$ and $\varepsilon_{\text{eff}} = -0.65\%$. Concerning the cabling parameters, it is assumed a cos(theta*)* = *0.97*. The input effective magnetic field is computed according to equation (1), starting from a 2D FE model of the total magnetic field on the conductor section, as described in section 4.1.

To obtain the MQE value, the power deposited in the strands was varied parametrically in the model, with steps of 25 W m^{-1} each. The results are summarized in figure 10. The MQE obtained for the 'TF-B' conductor is between 28 J (maximum recovery energy) and 29 J (i.e. 235 mJ cm^{-3} of cable). This value is about one order of magnitude larger than the measured one: 'TF-B' conductor showed indeed an unexpected behaviour (all quenches triggered at the same voltage of the capacitor bank, independent of the conductor temperature). Actually, it is very likely that the quench in that conductor was triggered by some defect or phenomena related to the flow obstruction between the He inlet and sensor P906, e.g. damage during the fabrication of the He inlet that reduces the current carrying capabilities of the strands in that region, acting as a quench initiator as soon as the inductive AC coil is fired. Therefore, the real MQE could be higher than the measured one, as suggested by the numerical analysis and more similar to that measured for the ITER CS [48, 50].

MQE simulations have also been carried out also for 'TF-A' conductor, resulting in a MQE value (see again figure 10) ∼50% lower than that of 'TF-B' conductor, as expected by the much higher *n-value* (13) measured in the DC tests of this conductor immediately before the MQE tests. Therefore, the measured deposited energy at 120–140 V should trigger a quench in 'TF-A'; however, it was never triggered experimentally because, as mentioned above, the 'TF-B' one always quenched unexpectedly at much lower energies (∼2–2.5 J).

4.4. Pressure drop test

The 'TF-B' conductor was instrumented with capillaries for pressure drop measurement on a 2 m distance. The measurements were carried out controlling the mass flow rate through the CV970 control valve at the 'TF-B' outlet; this allowed us to measure up to 9 steady state operating points, both at the beginning (BoC) and at the end (EoC) of EM cycles, as reported in figure 11. The raw SULTAN data (empty symbols) reported in figure 11(a) show a non-zero pressure drop at zero mass flow rate; that pressure drop was therefore considered an offset to be removed. At BoC, the maximum mass flow rate was limited by the above-mentioned flow obstruction at the inlet of 'TF-B': as reported in figure 11(c), when increasing the mass flow rate the outlet pressure reduced a lot, preventing the flow to reach 6 g s^{-1} even for an outlet pressure below 2 bar. Figure 11(c) also shows that an enormous and unusual pressure drop develops between the pressure measured by the 'P in R' sensor (see figure 3), *upstream* of the conductor inlet, and the P906 one, *immediately downstream* of the conductor inlet; therefore, there must be something blocking the flow close to the inlet region, due e.g. to ice formation during cool down or to defects during the soldering of the He inlet (or sample terminations). The same obstruction is reduced after the WUCD thermal cycles, allowing the total pressure to reach ∼8 g s^{-1} at the EoC, even though (see again figure 11(c)) the pressure drop across the inlet region of the 'TF-B' leg is still much higher than the overall pressure drop of the 'TF-A' leg. The reduction of the obstruction possibly leads also to an improvement of the flow characteristics by a factor ∼2 in the range of the nominal mass flow rate (2–4 g s^{-1}) that cannot therefore be attributed only to the void fraction redistribution after the EM cycles.

Figure 11(b) reports in dimensionless space the SULTAN measurements of the friction factor as a function of Reynolds number compared to the values obtained from the available correlations used in the thermal-hydraulic simulations. In particular, the analyses of the DTT TF magnets carried out with the 4 C code [5, 51, 52] adopted the modified Darcy-Forchheimer correlation [53, 54]. The latter falls in between the measured values of the friction factor at BoC and EoC in the operational range (2–4 g s^{-1}), proving to compute a conservatively higher pressure drop if compared to the more reliable EoC data (because it is collected without any obstruction at the conductor inlet). This qualifies the 4 C code hydraulic analyses, as clearly shown by the 4 C results obtained in figure 11 prescribing on a 2 m conductor model the P906 as inlet pressure and the P906—Δp value (see figure 3 for the name of the sensors) as outlet pressure, this allowed us to neglect the localized pressure drops in the SULTAN sample inlet/outlet regions and the distributed pressure drop of the helium pipes, prescribing more reliable boundary conditions.

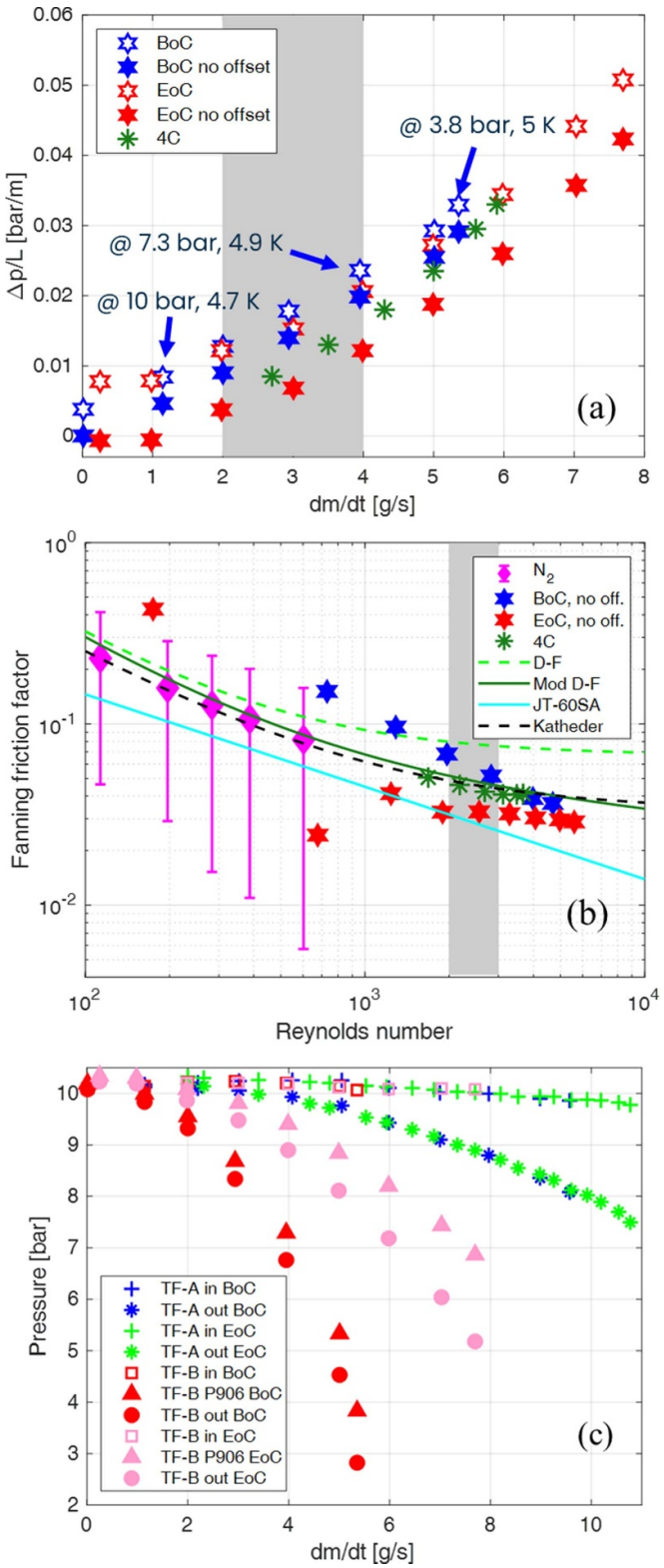

Figure 11. Dimensioned (a) and dimensionless (b) hydraulic characteristic of the 'TF-B' conductor. Data measured at beginning (BoC) and end (EoC) of EM cycles are reported, raw and without the offset of the pressure drop sensor. The measurements are compared with the 4 C code results and with several available friction factor correlations in (b): Darcy–Forchheimer (D–F) [53], modified Darcy–Forchheimer (Mod D–F) [54], correlation developed for JT-60SA (and W7-X) conductors [55], Katheder [56]. (c) Pressure measured at inlet and outlet of both legs at BoC and EoC during the hydraulic tests (for the 'TF-B' conductor, the pressure at P906 sensor is also reported, see figure 3 for its location). Outlet pressure measured during the sample tests and computing the mass flow rate.

5. Conclusions

The DTT TF SULTAN sample was manufactured with two 'legs' made of rectangular Wind & React CICCs, differing only for the twist pitches of the cabling stages. Reaction heat treatment, instrumentation installation and experimental tests have been carried out in SULTAN, at the Swiss Plasma Center.

The main objective of the tests was the verification of target design DC performance, and the experimental results have shown that the sample is able to sustain very large EM loads, exhibiting performances within design expectations. Up to 3000 EM loads and two WUCDs cycles have been applied. The final current sharing temperature measured at $I_{op} = 42.5$ kA—$B_{SULTAN} = 10.85$ T is 6.98 K for sample 'TF-A' and 6.36 K for sample 'TF-B'. Analysis of the results gives a clear indication in favour of the long twist pitch sequence of sample 'TF-A', as characterized by a long pitch at the first cabling stage, demonstrating that this sample presented negligible T_{cs} degradation and a rapid stabilization after very few EM load cycles.

AC losses on both legs were assessed by gas flow calorimetry and presented a significant reduction after cycling and WUCDs in conjunction with a shift of the peak to frequencies higher than 2 Hz. The $n\tau$ values, determined using the single time constant approximation, were found to be within acceptable values, i.e. ∼200–300 ms in virgin conditions, reduced by ∼1 order of magnitude after 200 EM load cycles and by another factor ∼2 after subsequent ∼3000 EM cycles.

Concerning the MQE tests, the measurements showed the quench onset to be at low energy (MQE ∼2 J) only in the TF-B conductor, always quenching at 140 V discharge from the AC inductive heater, independently from the He inlet temperature. Due to this unexpected behavior, a detailed assessment with the 4 C code was performed for both the TF-A and TF-B conductors, resulting in a computed MQE value of ∼14 J and ∼29 J, respectively, where the difference is mainly due to the different conductor *n-values*.

The measured hydraulic impedance (∼1.5 bar for 100 m of conductor, at ∼4 g s^{-1}) was in line with the predictions by the modified Darcy–Forchheimer correlation in the operational range (2–4 g s^{-1}), adopted in all the thermal-hydraulic analyses carried out with the 4 C code.

Data availability statement

The data cannot be made publicly available upon publication because they are owned by a third party and the terms of use prevent public distribution. The data that support the findings of this study are available upon reasonable request from the authors.

Acknowledgments

This paper, realized with the support of the DTT community, is largely based on the Italian proposal for DTT prepared with contributions of European and international experts [DTT—Divertor Tokamak Test Facility—Interim Design Report R Martone (Ed.) (2019) ISBN: 978-88-8286-378-4].

ORCID iDs

C Fiamozzi Zignani https://orcid.org/0000-0002-3632-2381
G De Marzi https://orcid.org/0000-0002-5752-2315
L Muzzi https://orcid.org/0000-0001-8465-3364
S Turtù https://orcid.org/0000-0002-5493-7785
A Zappatore https://orcid.org/0000-0001-7308-0273
K Sedlak https://orcid.org/0000-0002-2090-1709

References

[1] Ambrosino R 2021 DTT—Divertor Tokamak Test facility: a testbed for DEMO *Fusion Eng. Des.* **167** 112330
[2] Martone R, Albanese R, Crisanti F, Pizzuto A and Martin P eds 2019 DTT Divertor Tokamak Test facility, Interim Design Report *ENEA (ISBN 978–88-8286-378-4)*
[3] Federici G *et al* 2016 Overview of the design approach and prioritization of R & D activities towards an EU DEMO *Fus. Eng. Des.* **109–111** 1464–74
[4] Di Zenobio A *et al* 2022 DTT: a challenging framework for a sound superconducting magnets design *IEEE Trans. Appl. Supercond.* **32** 4201005
[5] Bonifetto R, Di Zenobio A, Muzzi L, Turtu S, Zanino R and Zappatore A 2020 Thermal-hydraulic analysis of the DTT toroidal field magnets in DC operation *IEEE Trans. Appl. Supercond.* **30** 4200605
[6] Smathers D, Flanigan J, Kim J and Sim K 2022 Niobium rod quality and its impact on the production of Nb_3Sn strand for the Divertor Tokamak Test facility toroidal coils *IOP Conf. Ser.: Mater. Sci. Eng.* **1241** 012017
[7] Uglietti D, Sedlak K, Wesche R, Bruzzone P, Muzzi L and Della Corte A 2018 Progressing in cable-in-conduit for fusion magnets: from ITER to low cost, high performance DEMO *Supercond. Sci. Technol.* **31** 055004
[8] Muzzi L, De Marzi G, Di Zenobio A and Della Corte A 2015 Cable-inconduit conductors: lessons from the recent past for future developments with low and high temperature superconductors *Supercond. Sci. Technol.* **28** 053001
[9] Nijhuis A and Ilyin Y 2006 Transverse load optimization in Nb_3Sn CICC design; influence of cabling, void fraction and strand stiffness *Supercond. Sci. Technol.* **19** 945–62
[10] Muzzi L *et al* E-WASP, a facility to test strain, temperature, magnetic field and current effects on superconducting samples *EUCAS 2017 Conf.* (available at: https://indico.cern.ch/event/659554/contributions/2716011/attachments/1527305/2388533/1MP1-06_Quagliata_Tamisari_Federico.pdf)
[11] Bottura L and Bordini B 2009 J_c(B,T,ε) parameterization for the ITER Nb_3Sn production *IEEE Trans. Appl. Supercond.* **19** 1521–4
[12] De Marzi G *et al* 2023 Electromechanical characterization of advanced internal-Tin Nb_3Sn strands for the DTT magnet system *IEEE Trans. Appl. Supercond.* **33** 1–5
[13] Nijhuis A, van Lanen E P A and Rolando G 2012 Optimization of ITER Nb_3Sn CICCs for coupling loss, transverse electromagnetic load and axial thermal contraction *Supercond. Sci. Technol.* **25** 015007
[14] Dixon I, Affinito L, Bird M D, Della Corte A, Hoffmann M, Painter T A, Polli G M, Roveta G, Roveta M and Smeibidl P 2012 Cable-in-conduit conductor fabrication for the series-connected hybrid magnets *IEEE Trans. Appl. Supercond.* **22** 4301004

[15] Bruzzone P*et al* 2002 User specification for conductor samples to be tested in the SULTAN facility (SULTAN-Team)

[16] Bruzzone P, Wesche R, Stepanov B, Cau F, Bagnasco M, Calvi M, Herzog R and Vogel M 2009 Qualification tests and facilities for the ITER superconductors *Nucl. Fusion* **49** 065034

[17] Breschi M, Carati D, Bessette D, Devred A, Romano G, Vostner A and Zhou C 2015 Performance analysis of the Nb−Ti conductor qualification samples for the ITER project *Supercond. Sci. Technol.* **28** 115001

[18] Breschi M, Macioce D and Devred A 2017 Performance analysis of the toroidal field ITER production conductors *Supercond. Sci. Technol.* **30** 055007

[19] Fiamozzi Zignani C, Muzzi L, Augieri A, Corato V, Della Corte A, De Marzi G, Bruzzone P, Sedlak K, Stepanov B and Uglietti D 2019 Strain distribution in the Nb_3Sn rectangular wind and react conductor of the European DEMO project, determined by inductive measurements *Fusion Eng. Des.* **146** 1539–42

[20] Bruzzone P *et al* 2008 Results of a new generation of ITER TF conductor samples in SULTAN *IEEE Trans. Appl. Supercond.* **18** 459–62

[21] Breschi M, Bessette D and Devred A 2011 Evaluation of effective strain and *n*-value of ITER TF conductor samples *IEEE Trans. Appl. Supercond.* **21** 1969–73

[22] Taylor D M J and Hampshire D P 2005 Relationship between the *n*-value and critical current in Nb_3Sn superconducting wires exhibiting intrinsic and extrinsic behaviour *Supercond. Sci. Technol.* **18** S297–302

[23] Fiamozzi Zignani C *et al* 2011 The effect of strand bending on the voltage-current characteristic of Nb_3Sn cable-in conduit conductors *IEEE Trans. Appl. Supercond.* **21** 3

[24] Mitchell N, Breschi M and Tronza V 2020 The use of Nb_3Sn in fusion: lessons learned from the ITER production including options for management of performance degradation *Supercond. Sci. Technol.* **33** 054007

[25] Fiamozzi Zignani C, Corato V, Muzzi L and Della Corte A 2010 Numerical simulation of Nb_3Sn strands performances with bending strain and comparison with experimental measurements *IEEE Trans. Appl. Supercond.* **20** 1432–5

[26] Muzzi L *et al* 2008 Performance enhancement under bending strain of Nb_3Sn strands with untwisted filaments *J. Appl. Phys.* **103** 073915

[27] COMSOL AB COMSOL multiphysics v. 6.1. (available at: www.comsol.com)

[28] Bruzzone P, Stepanov B and Wesche R 2006 Transverse load degradation in Nb_3Sn cable-in-conduit conductors with different cable pattern *AIP Conf. Proc.* **824** 558

[29] Bajas H 2011 Numerical simulation of the mechanical behavior of the ITER cable-in-conduit conductors *Ecole Centrale Paris* English ⟨NNT: 2011ECAP0016⟩. ⟨tel-00697000⟩

[30] Calzolaio C, Bruzzone P and Uglietti D 2012 Measurement of Tc distribution in Nb_3Sn CICC *Supercond. Sci. Technol.* **25** 054007

[31] Riccioli R, Torre A, Durville D, Breschi M and Lebon F 2022 Mechanical analysis of full-scale Nb_3Sn CICC designs for tokamaks *IEEE Trans. Appl. Supercond.* **32** 1–5

[32] Fiamozzi Zignani C *et al* 2022 DC characterization of a low-field Nb_3Sn prototype conductor for a DEMO TF coil *IEEE Trans. Appl. Supercond.* **32** 6

[33] Della Corte A *et al* 2010 Successful performances of the EU-AltTF sample, a large size Nb_3Sn cable-in-conduit conductor with rectangular geometry *Supercond. Sci. Technol.* **23** 045028

[34] Muzzi L *et al* 2017 Design, manufacture, and test of an 80 kA-class Nb_3Sn cable-in-conduit conductor with rectangular geometry and distirbuted pressure relief channels *IEEE Trans. Appl. Supercond.* **27** 1–6

[35] Turtù S, Muzzi L, Fiamozzi Zignani C, Corato V, Della Corte A, Di Zenobio A and Reccia L 2011 Role of the cross section geometry in rectangular Nb_3Sn CICC performances *IEEE Trans. Appl. Supercond.* **21** 2032

[36] Bruzzone P *et al* 2007 Test results of two ITER TF conductor short samples using high current density Nb_3Sn strands *IEEE Trans. Appl. Supercond.* **17** 1370–3

[37] Ciazynski D 2007 Review of Nb_3Sn conductors for ITER *Fusion Eng. Des.* **82** 488–97

[38] Dixon I R, Bird M D, Bruzzone P, Gavrilin A V, Lu J, Stepanov B and Weijers H W 2009 Current sharing and AC loss measuremetns of a cable-inconduit conductor with Nb_3Sn strands for the high field section of the series-connected hybrid outsert coil *IEEE Trans. Appl. Supercond.* **19** 2466–9

[39] Duchateau J C, Turk B, Torre A and Zani L 2021 An analytical model for coupling losses in large conductors for magnetic fusion *Cryogenics* **120** 103374

[40] Anvar V A, Qin J, Wu Y, Bagni T, Devred A, Haugan T J, Hossain M S A, Zhou C and Nijhuis A 2020 AC loss and contact resistance of different CICC cable patterns: experiments and numerical modeling *Fusion Eng. Des.* **161** 111898

[41] Muzzi L *et al* 2021 Design and characterization of the interlayer joint between low-field Nb_3Sn conductors of a layer wound DEMO TF coil *IEEE Trans. Appl. Supercond.* **31** 1–7

[42] Nijhuis A, ten Kate H H J, Duchateau J L and Bruzzone P 1996 Coupling loss time constants in full-size Nb_3Sn CIC model conductors for fusion magnets *Adv. Cryog. Eng. Mater.* **42** 1281–8

[43] Turck B and Zani L 2010 A macroscopic model for coupling current losses in cables made of multistages of superconducting strands and its experimental validation *Cryogenics* **50** 443–9

[44] Wilson M N 1987 *Superconducting Magnets* (Clarendon)

[45] Bruzzone P *et al* 2008 Test results of two European ITER TF conductor samples in SULTAN *IEEE Trans. Appl. Supercond.* **18** 1088–91

[46] ITER 2009 *Design Description Document 2009 DDD11-7:Conductors ITER D 2NBKXY v1.2* (SeptemberE. W.)

[47] Lemmon I H B, Huber M L and Mc Linden M O Reference fluid thermodynamic and transport properties *NIST Standard Reference Database 23* version 10.2018

[48] Bagni T, Duchateau J L, Breschi M, Devred A and Nijhuis A 2017 Analysis of ITER NbTi and Nb_3Sn CICCs experimental minimum quench energy with JackPot, MCM and THEA models *Supercond. Sci. Technol.* **30** 095003

[49] Muzzi L *et al* 2010 The JT-60SA toroidal field conductor reference sample: manufacturing and test results *IEEE Trans. Appl. Supercond.* **20** 442–6

[50] Savoldi L, Bonifetto R, Breschi M, Isono T, Martovetsky N, Ozeki H and Zanino R 2017 Analysis of the ITER central solenoid insert (CSI) coil stability tests *Cryogenics* **85** 8–14

[51] Richard L S, Casella F, Fiori B and Zanino R 2010 The 4C code for the cryogenic circuit conductor and coil modeling in ITER *Cryogenics* **50** 167–76

[52] Bonifetto R, De Bastiani M, Di Zenobio A, Muzzi L, Turtu S, Zanino R and Zappatore A 2022 Analysis of the thermal-hydraulic effects of a plasma disruption on the DTT TF magnets *IEEE Trans. Appl. Supercond.* **32** 4204007
[53] Bagnasco M, Bottura L and Lewandowska M 2010 Friction factor correlation for CICC's based on a porous media analogy *Cryogenics* **50** 711–9
[54] Lewandowska M and Bagnasco M 2011 Modified friction factor correlation for CICC's based on a porous media analogy *Cryogenics* **51** 541–5
[55] Wanner M 2009 Pressure drop of the W7-X cable-in-conduit conductor *JT60SA Report* AST D 2234VD1.1
[56] Katheder H 1994 Optimum thermohydraulic operation regime for cable-in-conduit superconductors *Cryogenics* **34** 595–8